Technical Note

On the 3D Reconstruction of Coastal Structures by Unmanned Aerial Systems with Onboard Global Navigation Satellite System and Real-Time Kinematics and Terrestrial Laser Scanning

Diogo Gonçalves [1,2,*], **Gil Gonçalves** [1,3], **Juan Antonio Pérez-Alvávez** [4] **and Umberto Andriolo** [1]

1   INESC Coimbra, Department of Electrical and Computer Engineering, Polo 2, 3030-290 Coimbra, Portugal; gil@mat.uc.pt (G.G.); uandriolo@mat.uc.pt (U.A.)
2   Department of Civil Engineering, University of Coimbra, 3030-788 Coimbra, Portugal
3   Department of Mathematics, University of Coimbra, 3001-501 Coimbra, Portugal
4   Departamento de Expresión Gráfica, Centro Universitario de Mérida, Universidad de Extremadura, 06800 Mérida (Badajoz), Spain; japerez@unex.es
*   Correspondence: diogo.goncalves@mat.uc.pt

Academic Editors: José Juan de Sanjosé Blasco, Germán Flor-Blanco and Ramón Blanco Chao

Publisher's Note: MDPI stays neutral with regard to jurisdictional claims in published maps and institutional affiliations.

Abstract: A wide variety of hard structures protect coastal activities and communities from the action of tides and waves worldwide. It is fundamental to monitor the integrity of coastal structures, as interventions and repairs may be needed in case of damages. This work compares the effectiveness of an Unmanned Aerial System (UAS) and a Terrestrial Laser Scanner (TLS) to reproduce the 3D geometry of a rocky groin. The Structure-from-Motion (SfM) photogrammetry technique applied on drone images generated a 3D point cloud and a Digital Surface Model (DSM) without data gaps. Even though the TLS returned a 3D point cloud four times denser than the drone one, the TLS returned a DSM which was not representing about 16% of the groin (data gaps). This was due to the occlusions encountered by the low-lying scans determined by the displaced rocks composing the groin. Given also that the survey by UAS was about eight time faster than the TLS, the SFM-MV applied on UAS images was the most suitable technique to reconstruct the rocky groin. The UAS remote sensing technique can be considered a valid alternative to monitor all types of coastal structures, to improve the inspection of likely damages, and to support coastal structure management.

Keywords: drone; groin; breakwater; structure from motion; 3D point cloud

1. Introduction

In the coastal environment, a wide variety of hard structures protect coastal activities and communities from the action of tides and waves worldwide [1–3]. Structure types have different configurations and constitution. Seawalls are built parallel to the shore to defend the inland areas and prevent shoreline retreatment [3,4]. Detached breakwaters are built shore parallel to dissipate wave energy in the nearshore [3], while jetties and shore-connected breakwaters play the function of protecting harbours and creating a secure environment for mooring, operating, and handling ships [3,5]. Finally, groins are built shore-perpendicular to mitigate shoreline erosion and intersect the updrift sediments [1,6]. Even though different materials can be used to build coastal structures, most of them are constituted by rocks and/or concrete [1,7].

It is fundamental to monitor the integrity of coastal structures and to detect likely damaged areas, to support management in the proposal of possible intervention and repairs. For instance, the displacement of stone blocks on rocky groins, rubble mound shore-connected breakwaters and jetties may endanger the stability of the structures, lowering and even compromising their protection functions [1,8,9]. The traditional monitoring methods of rocky coastal structures are based on visual or photographic inspections, however these

needs to be performed by qualified and trained personnel, and are technically, logistically and temporally limited [10–12]. Topographic surveys by totals stations and Global Navigation Satellite System (GNSS) have also been used, nevertheless, despite their advantages in terms of spatial accuracy, these methods require intense human effort in the field, and often do not provide a complete survey of the structure [12]. Recently, remote sensing techniques have been applied to monitor coastal structures. Aerial and terrestrial Light Detection and Ranging (LiDAR) can provide a detailed 3D reconstruction of rocky coastal protections [13], however the expensive costs and logistical constraints of LiDAR deployment remain the biggest disadvantages of this method.

A valuable alternative for monitoring coastal structures is the use Unmanned Aerial System (UAS). UAS can operate autonomously, provide high spatial and temporal resolution with relatively low-cost, and are viable tools for many operational tasks [14,15]. Given their adaptable and multipurpose properties, UASs have improved the coastal environmental monitoring to advance knowledge on beach–dune morphodynamics [16–23], coastal cliffs [24–26], and marine pollution [27–34], among others. The 3D reconstruction workflow consists in applying the Structure-from-Motion (SfM) photogrammetry techniques to UAS image bulk, to obtain a 3D dense point cloud representing the targeted area [35]. The use of Ground Control Points (GCPs) is needed to georeference the 3D dense point cloud [36], however a Real-Time Kinematic assisted UAS (e.g., DJI Phantom 4 RTK; UAS-RTK) can accurately estimate the camera position, thus the use of GCPs can be potentially avoided [37].

The 3D reconstruction of coastal structures with SfM photogrammetry may improve the knowledge of structural condition of armour layer for assessing the structure integrity over a time interval or after extreme events [1]. According to the Construction Industry Research and Information Association (CIRIA), there are four levels of measures to assess the condition of armour units [1]: (i) locate units movements by measure with GNSS survey; (ii) geometric survey to describe armour layer with similar technique of level I; (iii) armour units position and areas where core and underlayer are exposed using of photographic methods (photogrammetry, comparative photography); (iv) shape and size of armour units including armour fractures. Even though different parameters can characterize the geometry of armour layer, the most important ones are the packing density (number of units per area) and the armour layer porosity (proportion of void per volume) [1]. These two parameters have a close relationship and mainly affect the performance of the coastal structure [38].

Previous works on the 3D reconstruction of coastal structures with UAS-based imagery are limited to few examples, which focused on the accuracy evaluation of SfM photogrammetry product [39–41]. The positional accuracy of Digital Surface Model (DSM) in respect to GNSS receiver was assessed by Henriques et al. [39], who obtained 10 cm and 8 cm of horizontal and vertical accuracies, respectively. González-Jorge et al. [40] tested instead the performance of 3D point cloud for detecting displacements of armour layer units. Overall, these pioneering and preliminary works showed that UAS surveys can improve the inspection of coastal structures. However, this technique still needs to be better evaluated.

The aim of this paper is to assess the effectiveness of UAS-RTK and TLS techniques to reproduce the 3D geometry of a rocky groin. Two surveys were conducted at Leirosa beach on the North Atlantic Portuguese coast. The L-shape groin was digitally reconstructed by 3D point clouds and DSM. We evaluated the reconstruction of a L-shaped rocky groin by SfM photogrammetry and TLS scans in terms of mean surface density and data gaps. Overall, this work evaluates the most suitable technique to monitor the armour layer of coastal structures, such as groins and breakwaters, to improve the inspection of likely damages and support coastal management.

2. Methods

2.1. Study Site

The study site was the Leirosa beach, on the wave-dominated high energetic North Atlantic Portuguese coast (Figure 1a). In this coastal sector, the mesotidal regime has an average amplitude of 2.10 m, reaching a maximum elevation of 4 m during spring tides [42]. The dominant wave regime comes from NW with average significant wave height (Hs) of 2 m and period from 7 s to 15 s [43]. Intense erosion occurred in the last decades, mainly caused by the littoral drift retention at the Mondego estuary jetty, and by the decrease in sediment deposition from the Mondego river [44,45]. An average shoreline retreat of 2 m/year was registered by comparing satellite images from 1958 and 2010 [46], while the dune crest retracted of about 2 m southern the groin over 2018/2019 winter season [16]. An L-shaped rocky groin was built to protect the urban coastal agglomeration of Leirosa. The shore-perpendicular sector of the groin extends about 200 m, with an average elevation of 6 m above the mean sea level (MSL), while the shore-parallel sector is shorter (150 m) and slightly higher (7 m above MSL). Both sectors are composed by stone blocks of about 2.5 m with a shape factor of 60–80% and a mass of about 15 tonnes. Since the main longshore transport on this coast is oriented N-S [42,44,45], the groin intersects sediment updrift, determining accumulation and shoreline advance northern the structure, in front of the urbanized area of Leirosa (Figure 1b). The mean slope on the shore-perpendicular sector is 21° (1:2.7 m) while on the shore- parallel wall is 30° (1:1.75 m—Figure 1j). An initial, cursory visual inspection revealed significant displacements of stone blocks at the two heads of the groin, which can determine further dislocation and the loss of the original shape and function of the structure (Figure 1c–f).
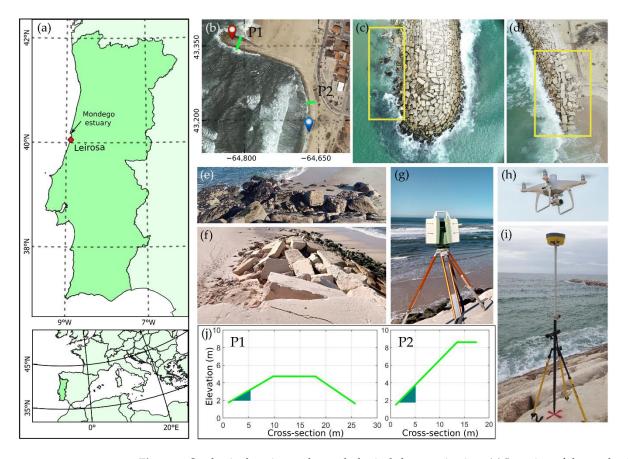

Figure 1. Study site location and morphological characterization. (**a**) Location of the study site and the Mondego estuary in Portugal; (**b**) Google satellite image of the groin in the local coordinate system (ETRS89/PT-TM06). Red and blue tags indicate the two heads of the groin shown in (**c,d**). Green lines indicate the two profiles shown in (**j**). (**c,d**) Pictures taken by DJI Phantom 4RTK showing

the two groin heads (namely, sub-area 1 and 3, see Section 2.4) (**e**,**f**) details of the two groin heads shown in (**c**,**d**), respectively; (**g–i**) equipment used in the fieldwork campaign, namely the Terrestrial Laser Scanning (TLS) Leica ScanStation C10 (**g**), the Unmanned Aerial System (UAS) DJI Phantom 4RTK (**h**) and the GeoMax Zenith 10 GNSS receiver (**i**); (**j**) two cross sections of the studied groin located in (**b**). Dark green triangles illustrate the slope of the berms.

A field work campaign was conducted with an Unmanned Aerial System (UAS) and a Terrestrial Laser Scanning (TLS) on 5 of November 2021 (Figure 1g–i). A dual frequency GNSS receiver was also used in Network Real Time Kinematic (NRTK) using the Portuguese stations ReNEP (https://renep.dgterritorio.gov.pt, accessed on 6 January 2022).to collect the coordinates of: (1) 13 control points to assess the Structure-from-Motion results (Section 2.2); and (2) 12 targets to georeference and co-register the TLS scans (Section 2.3).

2.2. Unmanned Aerial System Data Acquisition and Processing

The UAS survey was carried out with a DJI Phantom 4 RTK (P4RTK), equipped with a RGB camera (1″ CMOS sensor with 20 M effective pixels, 8.8 mm focal length and image size of 5472 × 3648 pixels). The setup of drone flight and cameras parameters was planned in DJI GST RTK, choosing a linear flight path (Figure 2a). The flight altitude was set to 50 m, considering an image overlap of 80% (both lateral and frontal). A total of 103 nadiral images was collected with a mean Ground Sample Distance (GSD) of 1.36 cm/pixel which is computed considering the flight altitude, sensor dimensions and focal length. The flight lasted about 10 min. Although the P4RTK can provide accurate georeferenced data [16,47], we drew 13 crosses on the blocks faces, evenly distributed along the groin, to evaluate the image positional accuracy in the post-processing phase. The measurements/collection of these points with the GNSS NRTK lasted about one hour.
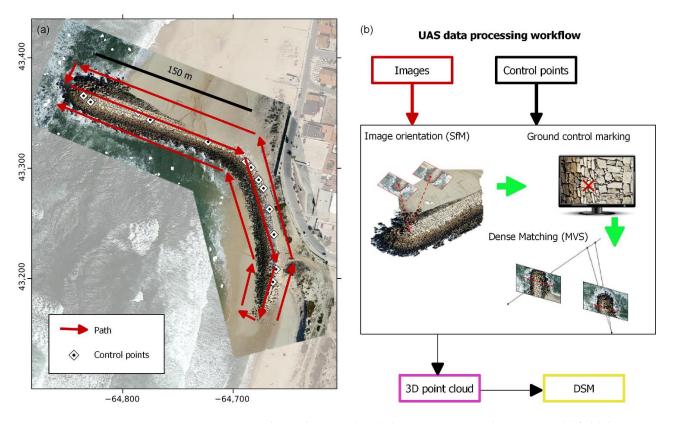

Figure 2. Unmanned Aerial System (UAS) data acquisition and processing. (**a**) field data acquisition represented on UAS orthophoto. Red arrows show the UAS flight path, white diamonds represent the control points placement for georeferencing process; (**b**) UAS data processing workflow: through structure from motion (SfM) and multi-view stereo technique (MVS), images and control points were processed for generating a 3D point cloud and a Digital Surface Model (DSM).

The UAS imagery post-processing phase was performed with Agisoft Metashape software. The application of SfM photogrammetry followed the workflow shown in Figure 2b. Firstly, images were oriented calculating the external and internal camera parameters through bundle block adjustment. A set of 3D points (tie points) was obtained representing the scale invariant features identified in overlapping images. Secondly, since the refinement of tie points improves the accuracy of reconstruction [26,48], we removed points with a reprojection error greater than 0.5. Afterwards, the bundle block adjustment was repeated using the refined tie points. Thirdly, the georeferencing process was performed by selecting only 3 ground control points from the set of 13 surveys points. The remaining 10 points were used as check points. All 13 control points were manually picked in the corresponding images. Fourthly, 3D point cloud was generated through dense matching by computer vision algorithms based on multi-stereoscopy (Figure 2b). Finally, after gridding the 3D point cloud with regular cells (i.e., squares 5×5 cm), we generated the DSM in CloudCompare. Each cell grid was calculated by the mean height of all points within the cell. The empty cells were linearly interpolated using the nearest cells.

2.3. Terrestrial Laser Scanning Data Acquisition and Processing

The TLS survey was performed with a Leica ScanStation C10, scan range of 300 m. The positional accuracy of a single TLS station is 6 mm for a range of 50 m. A total of seven scans were distributed along Leirosa groin, with most of stations chosen on the two groin heads (Figure 3a). A series of 12 circular targets were distributed in the TLS scan ranges of different station, to stich the scan data in the post-processing phase. Targets were placed among the terrain in order to be visible at least from two consecutive stations. Before starting the scanning procedure, targets were visually picked in the TLS screen, and measured with the GNSS NRTK receiver. When moving to the following station, we detected the same previous targets for building the scan network. During the TLS survey, the tide rose influencing the candidate zones for the scans position. In the end, the TLS survey lasted about 8 h.
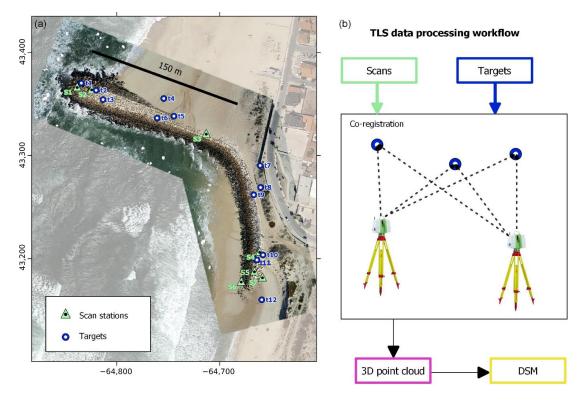

Figure 3. Terrestrial Laser Scanning (TLS) data acquisition and processing. (**a**) Field data acquisition on UAS orthophoto. Green triangles show the different stations in which the TLS was placed for

scanning (from 1 to 7), blue-white circles represent the targets (from 1 to 12) placed for stitching the scans acquired from different stations. (**b**) TLS data processing workflow: different scans are co-registered and joined using targets, for finally generating a 3D point cloud and a Digital Surface Model (DSM).

The resolution of scans was divided into the following categories: (i) medium resolution, corresponding to 10 cm distance between points at 100 m; (ii) high resolution, corresponding to 5 cm distance between points at 100 m.

The TLS post-processing methodology was performed with Leica Cyclone software (Figure 3b). The main steps consisted in: (i) importing the scans; (ii) reading targets coordinates; (iii) co-registration of the scans. The scans were stitched using the correspondent picked targets to produce a single 3D point cloud. The georeferencing process was also included, projecting the 3D point cloud into the Portuguese reference system. Using the same grid adopted to produce the UAS DSM (Section 2.2), we also generated the DSM from TLS 3D point cloud.

2.4. Three-Dimensional Point Clouds and Digital Surface Model

We evaluated and compared the 3D point clouds of both UAS-RTK and TLS using two quality parameters, namely the mean surface density and data gaps. We computed the two parameters for the entire groin structure, and for three sub-areas. Sub-areas were chosen on the groin heads and in the central groin area (Figure 4). The head on seaside is the more affected zone by waves, and already shows damages and block displacements. The south head shows also block displacements and covers the dune ridge, which is under severe erosion [16]. Finally, the central area represents a flat wall for protecting the urban area (see also Figure 1b–f).
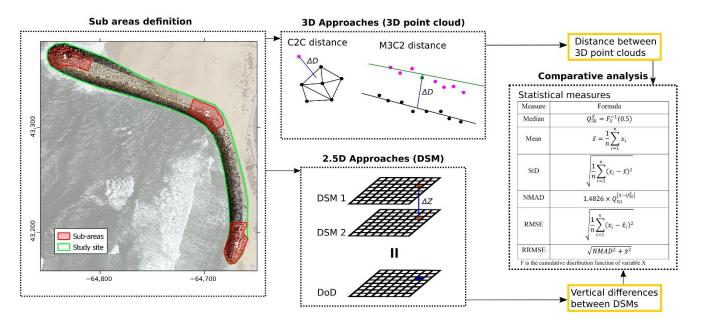

Figure 4. Data processing workflow for the comparative analysis. Three sub-areas (**left** box, red polygons) were defined over the whole groin structure (**left** box, green polygon). The distance between 3D point clouds and Digital Surface Model were computed using 3D and 2.5D approach based on point-to-point distance and vertical differences (**central** boxes). Finally, the errors were assessed through statistical measures computation (**right** box).

The mean surface density aims at characterizing the mean points concentration over the surface, identifying zones without points (data gaps). The 3D point clouds were projected along Z direction and converted into a regular grid. The mean surface density ($\bar{\rho}$)

was estimated by counting the points inside each grid cell and then calculating the mean of the overall cells density:

$$\bar{\rho} = \frac{1}{N} \sum_{i=1}^{N} c_i \qquad (1)$$

where N is the number of grid cells in the region of interest (C) and c_i is the point counting or local density in grid cell i.

The data gaps indicate the numbers of empty grid cells in the region of interest using

$$\delta_g = \#D_g \times A_c \qquad (2)$$

where $\#D_g$ is the cardinality of set $D_g = \{c_i : c_i = 0, \text{ for } i = 1, \dots, N\}$ formed by the empty grid cells and A_c is the grid area.

2.5. Comparative Analysis and Statistical Measures

To assess the accuracy and effectiveness of UAS-RTK and TLS products for mapping groins, we implemented a two-stage methodology (Figure 4): (i) 3D approach for assessing the positional accuracy of 3D point cloud, and (ii) 2.5 D approach for assessing the DSM vertical accuracy.

For the 3D approach, the distance between points of TLS and UAS was calculated. For this purpose, in CloudCompare software, two algorithms were adopted: (i) Cloud-to-Cloud (C2C) distance and (ii) Multiscale Model-to-Model Cloud Comparison (M3C2). The C2C computes directly the distance between two 3D point clouds based a local model fitting. This local model is calculated for each point of the reference data (TLS 3D point cloud) and is composed by: (1) the k nearest points or (2) the points inside a sphere with radius r of the target data (UAS 3D point cloud). The M3C2 measure computes the distances between two 3D point clouds through the normal direction of a local surface. This local surface is calculated by searching for points in a radius D and then a cylinder is computed along the normal direction that intersects the target data [49]. Therefore, the error of UAS point cloud (ΔD) was obtained by:

$$\Delta D = \begin{bmatrix} \Delta d_1 & \cdots & \Delta d_N \end{bmatrix} \qquad (3)$$

where Δd_i is the distance between the point i of UAS and the correspondent in TLS point cloud, and N is number of UAS 3D point cloud. Hereinafter, when ΔD is mentioned, it includes distances calculated by C2C and M3C2.

For the 2.5D approach, a direct vertical difference was calculated using DSM of Difference (DoD). The overall errors were obtained as:

$$\Delta Z = \begin{bmatrix} \Delta z_1 & \cdots & \Delta z_M \end{bmatrix} \qquad (4)$$

where $\Delta z_j = z_j^{TLS} - z_j^{UAS}$ is the vertical difference of j-th DoD cell.

Finally, the statistical analysis focused at characterizing the errors provided by the 3D and 2.5D approaches (Figure 4). We firstly fitted the histograms to characterize the distribution of errors. Then, a robust statistical analysis suitable for non-normal distributions was adopted [50], in order to compare the results with the traditional statistical measures. For traditional measures, the mean, the Standard Deviation (Std) and the Root Mean Square Error (RMSE) were calculated. For robust measures of non-normal error distributions, the median and Normalized Median Absolute Deviation (NMAD) were computed. In addition, the robust RMSE (RRMSE) was also computed based on mean and standard deviation [51].

3. Results

3.1. 3D Point Clouds and Digital Surface Model

The Agisoft Metashape processing workflow lasted about 1.5 h and returned a 3D point cloud with a georeferencing RMSE on check points equal to 3.2 cm. The 3D point cloud represented the entire groin with about 11 million points (Table 1), with a mean

surface density of 1.7×10^3 points/m^2 and without data gaps. After using the 12 targets to link the TLS scans in Cyclone that lasted about 1 h, the RMSE of TLS stitching was of 1.5 cm. The final 3D point cloud of TLS covered the groin with about 41 million points (Table 1). Even though the number of points and mean surface density of TLS point cloud was about three times the UAS one, the TLS data gap was about 16% of the entire groin area (6630 m^2).

Table 1. Characterization of the 3D point clouds obtained by the Unmanned Aerial System and Terrestrial Laser Scanning data. Number of points, mean surface density and data gaps are indicated for the whole groin structure and the three subareas (refer to Figure 4 for sub-areas identification).

	Parameters	Unmanned Aerial System	Terrestrial Laser Scanner
Whole structure (6630 m^2)	Number of points	11.3×10^6	41.3×10^6
	Mean surface density (points/m^2)	1.7×10^3	6.2×10^3
	Data gaps (%)	0	16.8
Sub-area 1 (560 m^2)	Number of points	1.0×10^6	15.2×10^6
	Mean surface density (points/m^2)	1.8×10^3	27.2×10^3
	Data gaps (%)	0	1.4
Sub-area 2 (530 m^2)	Number of points	0.9×10^6	0.7×10^6
	Mean surface density (points/m^2)	1.6×10^3	1.3×10^3
	Data gaps (%)	0	0
Sub-area 3 (600 m^2)	Number of points	1.2×10^6	21.8×10^6
	Mean surface density (points/m^2)	2.0×10^3	36.4×10^3
	Data gaps (%)	0	0.8

Overall, the number of points and mean surface density among the three sub-areas were much variable on TLS data, while did not change significantly for UAS. In fact, the mean surface density of TLS was higher on sub-areas 1 and 3, due to the more numerous scans and stations in these zones. Finally, for the sub-areas 1–3, which are the most interesting areas to be monitored on the groin structure, TLS survey returned an average 1.1% of surface data gaps. On the other hand, despite the lower means surface density, no data gaps were found on UAS survey. Figure 5 depicts the 3D point clouds and Digital Surface Models (DSM) obtained in the data processing step. Although the data gaps were present on TLS 3D points, the interpolation of the empty cells (5×5 cm) allowed to mitigate this effect on DSM.

3.2. Comparative Analysis and Statistical Measures of 3D Point Clouds and DSM

For analysing the spatial distribution of errors, Figure 6 shows the results of 3D and 2.5D approaches for the sub-areas. Overall, more than 50% of errors were concentrated between 0 and 10 cm. The accumulated green bars presented higher values in sub areas 1 and 3. In fact, the presence of data gaps was proportional to the increase of errors. The roughness of these sub-areas may have penalized the errors of M3C2 algorithm where it is not possible to compute the distance in several points due to wrong calculation of the normal direction of local surfaces (see Section 2.4 and Figure 4). The errors of sub-area 2 registered lower variability among the different algorithms. These results were due to the regular roughness of the groin surface. Overall, the non-normality of the errors distribution was corroborated with a course analysis of the histogram shapes. The main reason for this assumption is the right heavy tails of the histograms.
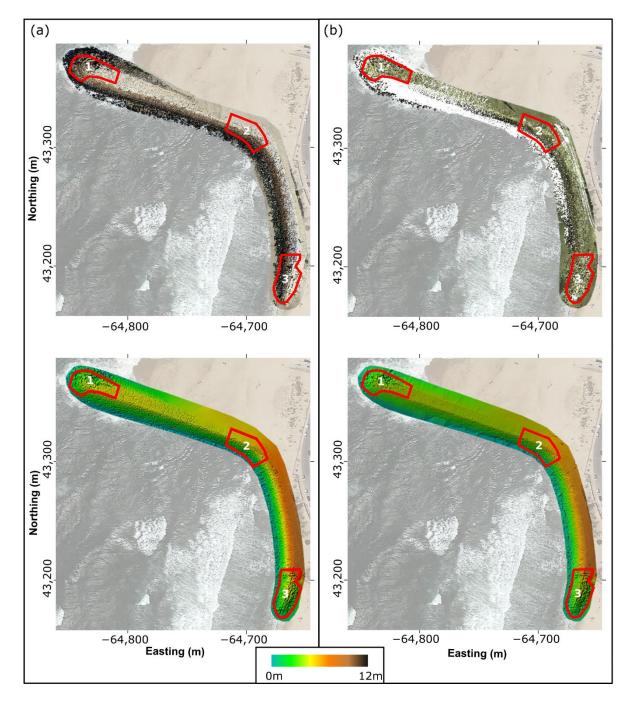
Figure 5. Products obtained by Unmanned Aerial System (**a**) and Terrestrial Laser Scanning (**b**). In details, 3D point clouds (upper row) and Digital Surface Models (DSM, lower row). Red numbered polygons represent the three chosen sub-areas (1–3, please refer to Section 2.4 for explanation). The axis labels refer to the projected Portuguese reference systems (ETRS89/PT-TM06).

For an in-depth assessment, the accuracy measures were tabulated highlighting the main differences between 3D and 2.5D approaches in sub-areas (Table 2). In general, the conventional measures overestimated the errors between UAS and TLS in comparison with the robust measures (in the worst case, differences were about 14 cm). The sub-area 2 presented the lower variability both in terms of Std and NMAD, while sub-area 1 showed high dispersion in relation to the mean value. Overall, the RMSE registered values in a range of 30 cm due to the variability of errors expressed in term of Std. In fact, the formulation of RMSE considers the square of errors that magnifies the largest values mainly observed in sub-areas 1 and 3. However, it can be observed that the RRMSE

presented a lower variability concentrating values in a range of 10 cm. Although the distribution of errors deviates from the normal distribution, the differences in sub-area 2 were not significant. Only M3C2 showed considerable deviations between RRMSE and RMSE (9 cm).
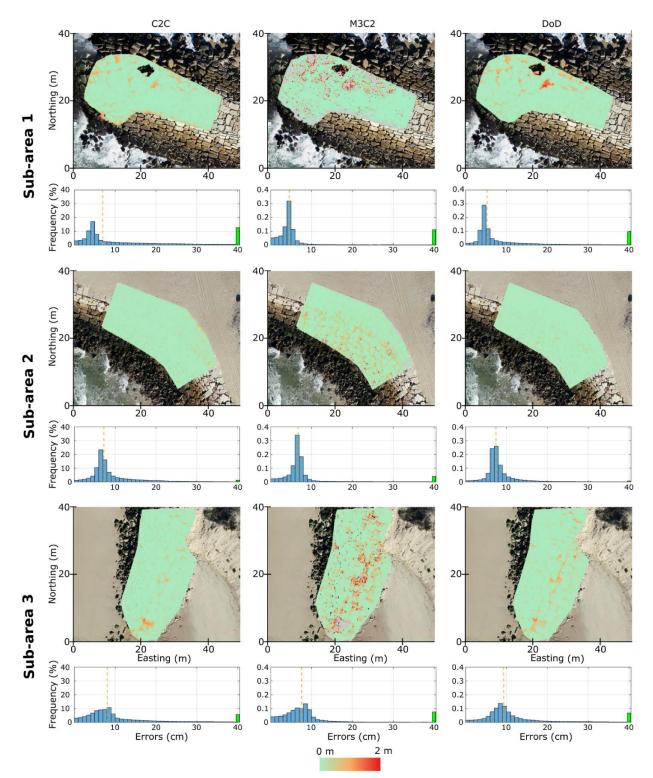

Figure 6. Spatial distribution of errors between Unmanned Aerial System and Terrestrial Laser Scanning for the three sub-areas (refer to Figure 4 for sub-area locations). In histograms, the vertical orange dashed lines represent the median value, green bars show the accumulated values greater than 40 cm).

Table 2. Statistical measures of 3D point cloud and DSM in the chosen sub-areas. Cloud-to-Cloud (C2C) and Multiscale Model-to-Model Cloud Comparison (M3C2) were the 3D approaches applied to the 3D point clouds. DSM of Differences (DoD) was the 2.5D approach applied to the DSM. The statistical measures were composed by: (i) traditional measures for normal distributions: mean, standard deviation (StD) and Root Mean Square Error (RMSE); (ii) robust measures for non-normal distributions: median, Normalized Mean Absolute Deviation (NMAD) and Robust RMSE (RRMSE). For the formulas of statistical measures, please refer to Figure 4.

Approach	Sub-Area	Mean (cm)	Median (cm)	Std (cm)	NMAD (cm)	RMSE (cm)	RRMSE (cm)
C2C	1	17.2	7.0	21.1	6.4	27.2	18.4
	2	10.0	7.2	7.9	2.3	12.7	10.3
	3	12.9	8.1	15.3	5.0	20.0	13.8
M3C2	1	16.8	4.6	36.0	1.6	39.8	16.9
	2	10.2	6.7	16.5	1.3	19.4	10.3
	3	14.4	7.6	26.8	3.5	30.4	14.8
DoD	1	14.9	5.3	23.8	2.3	28.1	15.0
	2	9.0	7.4	6.0	1.5	10.8	9.1
	3	14.5	9.3	16.1	3.8	21.7	15.0

4. Discussion

A Real-Time Kinematic assisted Unmanned Aerial System (UAS-RTK) and a Terrestrial Laser Scanning (TLS) were used to reconstruct a L-shape groin (Figure 1). The fieldwork task was much faster and easier with the UAS-RTK, since the drone flew and collected images autonomously in about 10 min. Even though flight planning and camera setup request a certain experience and expertise (Figure 2), the fieldwork was much less demanding than TLS deployment. In fact, the limited scan range of the TLS required to place, move and re-place the instrument through different positions and stations (Figure 3) to survey the entire structure. The task also required several re-placements of targets to further stitching the scans from different stations in the post-processing phase. Even though a single TLS scan lasted about 20 min, placing the instrument and the targets over the different stations, beside marking the targets in the TLS, lasted about six times the drone setup and deployment. On the other hand, UAS-RTK and TLS returned similar data processing times (1.5 h and 1 h, respectively) and requested similar experience and expertise. It is worth to highlight that the hardest task was to manually mark the 13 control points in images that lasted about 20 min.

We experienced some logistical limitations due to tide excursion and wave spray. As also observed by Medjkane et al. [52], it was necessary to plan the data acquisition during low tide to maximize the coverage of the structure, since the Portuguese coast is a meso-tidal environment with tide range up between 1.2 m and 3.6 m [42,44,45]. Due to the longer time data collection requested by the TLS, it was necessary to place the instrument far from the edges of the structure to guaranty the integrity of the equipment, whose data might have been affected by wave spray of breaking wave height at this high-energetic coast [43]. This constrains on TLS placement caused also the occlusion of several relevant zones affecting the data completeness mainly on downdrift areas (Figure 5). On the other hand, the drone deployment and quality of images can be limited by certain environmental conditions, since (i) wind speed should be less than 20 km/h, (ii) drone cannot fly during rainy days, and (iii) fog and mist are common on the Portuguese coast also during summer [16].

The advantages of UAS-RTK in comparison with TLS were also observed in the quantitative 3D reconstruction of the groin. The proposed quality parameters were crucial for assessing the effectiveness of these two techniques to reproduce the 3D geometry of a rocky groin. Even though UAS returned a 3D point cloud with number of points and mean surface density of a magnitude four times smaller, no data gaps were observed in the 3D reconstruction (Table 1). On the other hand, despite the high number of points and mean surface density, it was not possible to reconstruct about 16% of the groin structure (Table 1).

It is worth to highlight that the sub-areas 1 and 2 were chosen to allow the computation of the comparative statistics that require similar point distribution over the surface (Figure 6 and Table 2). In fact, the groin surface zone without TLS data was higher on these sub-areas (Figure 5) not covering the entire groin section. To further assessments of monitoring tasks (e.g., track armour units movements), these sub-areas should be upgraded to cover the entire section.

The proposed approaches for assessing the positional and vertical accuracies of UAS 3D point clouds and Digital Surface Models returned substantial differences between traditional and robust statistical measures. The armour units displayed on sub-areas 1 and 3 returned several outliers in M3C2 and C2C, due to the low mean surface density and the existence of data gaps on TLS data (Figure 6 and Table 2). A considerable proportion of voids on armour layer was observed on these sub-areas caused by the displacement of several armour units (Figure 1e,f). Due to the lower block density, the initial shape of the structure was modified and showed increased surface roughness complexity, which also influenced the M3C2 and C2C distance computation. On the other hand, the sub-area 2 returned low differences between traditional and robust measures, since this area was composed by more regular surface and stone blocks were more framed. In fact, a lower proportion of voids on armour layer was observed on this sub-area mitigating the impact of outliers in M3C2 and C2C distance computation.

When comparing similar works devoted to 3D reconstruction of coastal structure, we showed that the use of a Real-Time Kinematic assisted UAS (DJI Phantom 4 RTK) can improve the positional accuracy and the time-demanding placing and surveys of GCPs can be avoided. The error on check points was substantially lower (3.6 cm) than Henriques et al. [39], who obtained a DSM positional RMSE of 12.8 cm using a set of GCP and a traditional workflow.

The recent technological advances allow to incorporate a LiDAR sensor on drones, which have shown promising results when compared with the UAS-based imagery in terms of surface density [53]. However, the relative high cost for acquiring UAS-LiDAR suggests that UAS imagery combined with SfM photogrammetry is still a cost-effective and valuable solution to reproduce the 3D geometry of rubble mound groins. In fact, for this type of coastal structures with regular armour units (60–80% shape factor), this remote sensing technique could be used to characterize the armour layer geometry in terms of packing density and the armour layer porosity. However, for structures with more complex armour units (e.g., tetrapod) a further investigation should be implemented for analysing the impact of the armour layer roughness on the 3D reconstruction in terms of data gaps. The use of different flight plan configurations (combining nadiral and oblique images) could be an alternative to mitigate the existence of blind spots and improve the density 3D point cloud [54,55].

Since the use of UAS showed satisfactory results both in terms of data collection time and 3D reconstruction, the UAS imagery combined with SfM photogrammetry can be potentially used to: (i) develop a geospatial database of the coastal structures on the Portuguese coast; (ii) to increase the temporal resolution of data collection and explore the potentialities of simultaneous localization additional mapping (SLAM) to improve the efficiency of data processing [56,57]; (iii) improve the effectiveness of inspection; (iv) monitor the evolution of likely damaged areas; (v) create a framework to automatically segment the armour units for analysing and quantifying the damage areas [58]; (vi) provide an effective tool to the decision makers and coastal management entities.

5. Conclusions

This work reported a fieldwork campaign conducted with a Real-Time Kinematic assisted Unmanned Aerial System (UAS-RTK) and a Terrestrial Laser Scanning (TLS) to survey the 3D geometry of a rocky groin on the North Atlantic Portuguese coast.

The Structure-from-Motion (SfM) photogrammetry technique applied on drone images generated a 3D point cloud and a Digital Surface Model (DSM) without data gaps. The

drone setup and deployment lasted about one hour. The TLS returned a 3D point cloud four times denser than the drone, however the resulting DSM was not representing about 16% of the groin (data gaps). This was due to the occlusions encountered by the low-lying scans determined by the displaced rocks composing the groin. Given that the survey by TLS was about three times slower than the UAS-RTK, the SFM-MVS applied on UAS-RTK images was the most suitable technique to reconstruct the rocky groin.

The UAS-RTK remote sensing technique can be used a valid alternative to monitor rubble mound groins with a shape factor of the armour units between 60–80%. Unlike TLS, UAS-RTK can map the roughness of the armour layer including areas with high armour porosity mainly caused by the displacements of armour units. The drone deployment and the SfM applied on images can improve the inspection of likely damages of coastal structures, to support coastal structure management and interventions. Future works could be focus on testing different flight plan configuration to 3D reconstruct the geometry of other coastal structures with lower shape factor of the armour units and with more complex surface roughness.

References

1. CIRIA; CUR; CETMEF. *The Rock Manual. The Use of Rock in Hydraulic Engineering*, 2nd ed.; C683; CIRIA: London, UK, 2007; ISBN 9780860176831.
2. U.S. Army Corps of Engineers. *Coastal Engineering Manual (EM 1110-2-1100)*; U.S. Army Corps of Engineers: Washington, DC, USA, 2002.
3. Kamphuis, J.W. *Introduction to Coastal Engineering and Management*; World Scientific: Singapore, 2000; ISBN 981-02-3830-4.
4. Oliveira, J.N.C.; Oliveira, F.S.B.F.; Neves, M.G.; Clavero, M.; Trigo-Teixeira, A.A. Modeling wave overtopping on a seawall with XBeach, IH2VOF, and mase formulas. *Water* **2020**, *12*, 2526. [CrossRef]
5. Reis, M.T.; Neves, M.G.; Lopes, M.R.; Hu, K.; Silva, L.G. Rehabilitation of sines west breakwater: Wave overtopping study. *Proc. Inst. Civ. Eng. Marit. Eng.* **2011**, *164*, 15–32. [CrossRef]
6. Santos, C.J.; Andriolo, U.; Ferreira, J.C. Shoreline response to a sandy nourishment in a wave-dominated coast using video monitoring. *Water* **2020**, *12*, 1632. [CrossRef]
7. Allen, R.T. *Concrete in Coastal Structures*; Thomas Telford: London, UK, 1998.
8. Isobe, M. Impact of global warming on coastal structures in shallow water. *Ocean Eng.* **2013**, *71*, 51–57. [CrossRef]

9. Dos Reis, M.T.L.G.V.; Poseiro, P.G.G.; Fortes, C.J.E.M.; Conde, J.M.P.; Didier, E.L.; Sabino, A.M.G.; Grueau, M.A.S.R. Risk management in maritime structures. In Proceedings of the Eighth International Conference on Management Science and Engineering Management: Focused on Computing and Engineering Management, Lisbon, Portugal, 25–27 July 2014; Volume 281, pp. 1179–1190.

10. Santos, J.A.; Neves, M.D.G.; Silva, L.G. Rubble-mound breakwater inspection in Portugal. In Proceedings of the Coastal Structures 2003, Portland, OR, USA, 26–30 August 2003; pp. 249–261.

11. Silvestre, C.; Oliveira, P.; Pascoal, A.; Sebastião, L.; Alves, J.; Santos, J.A.; Silva, L.G.; Neves, M.D.G. Inspection and Diagnosis of Sines' West Breakwater. *Coast. Eng.* **2005**, *4*, 3555–3567.

12. Lemos, R.; Capitão, R.; Fortes, C.; Henriques, M.; Silva, L.G.; Martins, T. A methodology for the evaluation of evolution and risk of breakwaters. Application to Portimão harbor and of Faro-Olhão inlet. *J. Integr. Coast. Zone Manag.* **2020**, *20*, 103–119. [CrossRef]

13. Puente, I.; Sande, J.; González-Jorge, H.; Peña-González, E.; Maciñeira, E.; Martínez-Sánchez, J.; Arias, P. Novel image analysis approach to the terrestrial LiDAR monitoring of damage in rubble mound breakwaters. *Ocean Eng.* **2014**, *91*, 273–280. [CrossRef]

14. Tmušić, G.; Manfreda, S.; Aasen, H.; James, M.R.; Gonçalves, G.; Ben-Dor, E.; Brook, A.; Polinova, M.; Arranz, J.J.; Mészáros, J.; et al. Current practices in UAS-based environmental monitoring. *Remote Sens.* **2020**, *12*, 1001. [CrossRef]

15. Manfreda, S.; Mccabe, M.F.; Miller, P.E.; Lucas, R.; Pajuelo, V.M.; Mallinis, G.; Ben Dor, E.; Helman, D.; Estes, L.; Ciraolo, G.; et al. Use of Unmanned Aerial Systems for Environmental Monitoring. *Remote Sens.* **2018**, *10*, 641. [CrossRef]

16. Andriolo, U.; Gonçalves, G.; Sobral, P.; Fontán-Bouzas, Á.; Bessa, F. Beach-dune morphodynamics and marine macro-litter abundance: An integrated approach with Unmanned Aerial System. *Sci. Total Environ.* **2020**, *749*, 141474. [CrossRef]

17. Duo, E.; Chris Trembanis, A.; Dohner, S.; Grottoli, E.; Ciavola, P. Local-scale post-event assessments with GPS and UAV-based quick-response surveys: A pilot case from the Emilia-Romagna (Italy) coast. *Nat. Hazards Earth Syst. Sci.* **2018**, *18*, 2969–2989. [CrossRef]

18. Duo, E.; Fabbri, S.; Grottoli, E.; Ciavola, P. Uncertainty of drone-derived dems and significance of detected morphodynamics in artificially scraped dunes. *Remote Sens.* **2021**, *13*, 1823. [CrossRef]

19. Fairley, I.; Horrillo-Caraballo, J.; Masters, I.; Karunarathna, H.; Reeve, D.E. Spatial variation in coastal dune evolution in a high tidal range environment. *Remote Sens.* **2020**, *12*, 3689. [CrossRef]

20. Bastos, A.P.; Lira, C.P.; Calvão, J.; Catalão, J.; Andrade, C.; Pereira, A.J.; Taborda, R.; Rato, D.; Pinho, P.; Correia, O. UAV Derived Information Applied to the Study of Slow-changing Morphology in Dune Systems. *J. Coast. Res.* **2018**, *85*, 226–230. [CrossRef]

21. Taddia, Y.; Corbau, C.; Zambello, E.; Pellegrinelli, A. UAVs for structure-from-motion coastal monitoring: A case study to assess the evolution of embryo dunes over a two-year time frame in the po river delta, Italy. *Sensors* **2019**, *19*, 1717. [CrossRef] [PubMed]

22. Luppichini, M.; Bini, M.; Paterni, M.; Berton, A.; Merlino, S. A new beach topography-based method for shoreline identification. *Water* **2020**, *12*, 3110. [CrossRef]

23. Gonçalves, G.; Santos, S.; Duarte, D.; Gomes, J. Monitoring Local Shoreline Changes by Integrating UASs, Airborne LiDAR, Historical Images and Orthophotos. In Proceedings of the 5th International Conference on Geographical Information Systems Theory, Applications and Management, Crete, Greece, 3–5 May 2019; Scitepress—Science and Technology Publications: Setúbal, Portugal; pp. 126–134.

24. Jaud, M.; Letortu, P.; Théry, C.; Grandjean, P.; Costa, S.; Maquaire, O.; Davidson, R.; Le Dantec, N. UAV survey of a coastal cliff face—Selection of the best imaging angle. *Meas. J. Int. Meas. Confed.* **2019**, *139*, 10–20. [CrossRef]

25. Gómez-Gutiérrez, Á.; Gonçalves, G.R. Surveying coastal cliffs using two UAV platforms (multi-rotor and fixed- wing) and three different approaches for the estimation of volumetric changes. *Int. J. Remote Sens.* **2020**, *41*, 8143–8175. [CrossRef]

26. Gonçalves, G.; Gonçalves, D.; Gómez-gutiérrez, Á.; Andriolo, U.; Pérez-alvárez, J.A. 3d reconstruction of coastal cliffs from fixed-wing and multi-rotor uas: Impact of sfm-mvs processing parameters, image redundancy and acquisition geometry. *Remote Sens.* **2021**, *13*, 1222. [CrossRef]

27. Andriolo, U.; Gonçalves, G.; Sobral, P.; Bessa, F. Spatial and size distribution of macro-litter on coastal dunes from drone images: A case study on the Atlantic coast. *Mar. Pollut. Bull.* **2021**, *169*, 112490. [CrossRef] [PubMed]

28. Duarte, D.; Andriolo, U.; Gonçalves, G. Addressing the Class Imbalance Problem in the Automatic Image Classification of Coastal Litter From Orthophotos Derived From Uas Imagery. *ISPRS Ann. Photogramm. Remote Sens. Spat. Inf. Sci.* **2020**, *3*, 439–445. [CrossRef]

29. Andriolo, U.; Gonçalves, G.; Rangel-Buitrago, N.; Paterni, M.; Bessa, F.; Gonçalves, L.M.S.; Sobral, P.; Bini, M.; Duarte, D.; Fontán-Bouzas, Á.; et al. Drones for litter mapping: An inter-operator concordance test in marking beached items on aerial images. *Mar. Pollut. Bull.* **2021**, *169*, 112542. [CrossRef] [PubMed]

30. Gonçalves, G.; Andriolo, U.; Pinto, L.; Bessa, F. Mapping marine litter using UAS on a beach-dune system: A multidisciplinary approach. *Sci. Total Environ.* **2020**, *706*, 135742. [CrossRef]

31. Gonçalves, G.; Andriolo, U.; Gonçalves, L.; Sobral, P.; Bessa, F. Quantifying Marine Macro Litter Abundance on a Sandy Beach Using Unmanned Aerial Systems and Object-Oriented Machine Learning Methods. *Remote Sens.* **2020**, *12*, 2599. [CrossRef]

32. Taddia, Y.; Corbau, C.; Buoninsegni, J.; Simeoni, U.; Pellegrinelli, A. UAV Approach for Detecting Plastic Marine Debris on the Beach: A Case Study in the Po River Delta (Italy). *Drones* **2021**, *5*, 140. [CrossRef]

33. Andriolo, U.; Garcia-garin, O.; Vighi, M.; Borrell, A.; Gonçalves, G. Beached and Floating Litter Surveys by Unmanned Aerial Vehicles: Operational Analogies and Differences. *Remote Sens.* **2022**, *14*, 1336. [CrossRef]

34. Gonçalves, G.; Andriolo, U. Operational use of multispectral images for macro-litter mapping and categorization by Unmanned Aerial Vehicle. *Mar. Pollut. Bull.* **2022**, *176*, 113431. [CrossRef] [PubMed]

35. Smith, M.W.; Carrivick, J.L.; Quincey, D.J. Structure from motion photogrammetry in physical geography. *Prog. Phys. Geogr.* **2015**, *40*, 247–275. [CrossRef]

36. Taddia, Y.; González-García, L.; Zambello, E.; Pellegrinelli, A. Quality Assessment of Photogrammetric Models for Façade and Building Reconstruction Using DJI Phantom 4 RTK. *Remote Sens.* **2020**, *12*, 3144. [CrossRef]

37. Štroner, M.; Urban, R.; Seidl, J.; Reindl, T.; Brouček, J. Photogrammetry Using UAV-Mounted GNSS RTK: Georeferencing Strategies without GCPs. *Remote Sens.* **2021**, *13*, 1336. [CrossRef]

38. Bosma, C.; Civiel, S.; Verhagen, H.J. Void porosity measurements in coastal structures. In *Coastal Engineering 2002*; World Scientific Publishing Company: Singapore, 2002; pp. 1411–1423. [CrossRef]

39. Henriques, M.J.; Fonseca, A.; Roque, D.; Lima, J.N.; Marnoto, J. Assessing the Quality of an UAV-based Orthomosaic and Surface Model of a Breakwater. 2014, pp. 1–16. Available online: https://mycoordinates.org/assessing-the-quality-of-an-uav-based-orthomosaic-and-surface-model-of-a-breakwater/ (accessed on 14 February 2022).

40. González-Jorge, H.; Puente, I.; Roca, D.; Martínez-Sánchez, J.; Conde, B.; Arias, P. UAV Photogrammetry Application to the Monitoring of Rubble Mound Breakwaters. *J. Perform. Constr. Facil.* **2016**, *30*, 04014194. [CrossRef]

41. King, S.; Leon, J.; Mulcahy, M.; Jackson, L.A.; Corbett, B. Condition survey of coastal structures using UAV and photogrammetry. In Proceedings of the Australasian Coasts & Ports conference, Cairns, Australia, 21–23 June 2017; pp. 704–710.

42. Mendes, D.; Pais-Barbosa, J.; Baptista, P.; Silva, P.A.; Bernardes, C.; Pinto, C. Beach Response to a Shoreface Nourishment (Aveiro, Portugal). *J. Mar. Sci. Eng.* **2021**, *9*, 1112. [CrossRef]

43. Andriolo, U.; Mendes, D.; Taborda, R. Breaking wave height estimation from timex images: Two methods for coastal video monitoring systems. *Remote Sens.* **2020**, *12*, 204. [CrossRef]

44. Fernández-Fernández, S.; Ferreira, C.C.; Silva, P.A.; Baptista, P.; Romão, S.; Fontán-Bouzas, Á.; Abreu, T.; Bertin, X. Assessment of dredging scenarios for a tidal inlet in a high-energy coast. *J. Mar. Sci. Eng.* **2019**, *7*, 395. [CrossRef]

45. Ferreira, C.; Silva, P.A.; Fernández-Fernández, S.; Baptista, P.; Abreu, T.; Romão, S.; Fontán-Bouzas, Á.; Bertin, X.; Garrido, C. Wave Climate Definition on Modeling Morphological Changes in Figueira da Foz Coastal System (W Portugal). *J. Coast. Res.* **2018**, *85*, 1256–1260. [CrossRef]

46. Ponte Lira, C.; Silva, A.N.; Taborda, R.; De Andrade, C.F. Coastline evolution of Portuguese low-lying sandy coast in the last 50 years: An integrated approach. *Earth Syst. Sci. Data* **2016**, *8*, 265–278. [CrossRef]

47. Taddia, Y.; Stecchi, F.; Pellegrinelli, A. Coastal Mapping Using DJI Phantom 4 RTK in Post-Processing Kinematic Mode. *Drones* **2020**, *4*, 9. [CrossRef]

48. Rangel, J.M.G.; Gonçalves, G.; Pérez, J.A. The impact of number and spatial distribution of GCPs on the positional accuracy of geospatial products derived from low-cost UASs. *Int. J. Remote Sens.* **2018**, *39*, 7154–7171. [CrossRef]

49. Lague, D.; Brodu, N.; Leroux, J. Accurate 3D comparison of complex topography with terrestrial laser scanner: Application to the Rangitikei canyon (N-Z). *ISPRS J. Photogramm. Remote Sens.* **2013**, *82*, 10–26. [CrossRef]

50. Höhle, J.; Höhle, M. Accuracy assessment of digital elevation models by means of robust statistical methods. *ISPRS J. Photogramm. Remote Sens.* **2009**, *64*, 398–406. [CrossRef]

51. Gonçalves, G.R.; Pérez, J.A.; Duarte, J. Accuracy and effectiveness of low cost UASs and open source photogrammetric software for foredunes mapping. *Int. J. Remote Sens.* **2018**, *39*, 5059–5077. [CrossRef]

52. Medjkane, M.; Maquaire, O.; Costa, S.; Roulland, T.; Letortu, P.; Fauchard, C.; Antoine, R.; Davidson, R. High-resolution monitoring of complex coastal morphology changes: Cross-efficiency of SfM and TLS-based survey (Vaches-Noires cliffs, Normandy, France). *Landslides* **2018**, *15*, 1097–1108. [CrossRef]

53. Lin, Y.-C.; Cheng, Y.-T.; Zhou, T.; Ravi, R.; Hasheminasab, S.M.; Flatt, J.E.; Troy, C.; Habib, A. Evaluation of UAV LiDAR for mapping coastal environments. *Remote Sens.* **2019**, *11*, 2893. [CrossRef]

54. Tu, Y.H.; Johansen, K.; Aragon, B.; Stutsel, B.M.; Angel, Y.; Camargo, O.A.L.; Al-Mashharawi, S.K.M.; Jiang, J.; Ziliani, M.G.; McCabe, M.F. Combining Nadir, Oblique, and Façade Imagery Enhances Reconstruction of Rock Formations Using Unmanned Aerial Vehicles. *IEEE Trans. Geosci. Remote Sens.* **2021**, *59*, 9987–9999. [CrossRef]

55. Rossi, P.; Mancini, F.; Dubbini, M.; Mazzone, F.; Capra, A. Combining nadir and oblique uav imagery to reconstruct quarry topography: Methodology and feasibility analysis. *Eur. J. Remote Sens.* **2017**, *50*, 211–221. [CrossRef]

56. Han, S.; Jiang, Y.; Bai, Y. Fast-PGMED: Fast and Dense Elevation Determination for Earthwork Using Drone and Deep Learning. *J. Constr. Eng. Manag.* **2022**, *148*, 04022008. [CrossRef]

57. Shang, Z.; Shen, Z. Real-time 3D reconstruction on construction site using visual SLAM and UAV. *Constr. Res. Congr. Constr. Inf. Technol.-Sel. Pap. Constr. Res. Congr.* **2018**, *2018*, 305–315. [CrossRef]

58. Valero, E.; Bosché, F.; Forster, A. Automatic segmentation of 3D point clouds of rubble masonry walls, and its application to building surveying, repair and maintenance. *Autom. Constr.* **2018**, *96*, 29–39. [CrossRef]